AIAA-2000-0897
FLAPPING-WING PROPULSION FOR A MICRO AIR VEHICLE

K.D.Jones and M.F.Platzer
Naval Postgraduate School
Monterey, CA

38th Aerospace Sciences Meeting & Exhibit
10-13 January 2000 / Reno, NV

FLAPPING-WING PROPULSION FOR A MICRO AIR VEHICLE

K. D. Jones[†] and M. F. Platzer[‡]

Naval Postgraduate School
Monterey, California

Abstract

Recent interest in the development of micro-air-vehicles (MAVs) has led to a renewed interest in flapping-wing propulsion due to the relatively poor efficiencies of conventional propellers at these small scales. In the present study flapping-wing configurations found numerically to produce high propulsive-efficiencies are investigated experimentally. Several models of varying scales and complexity are developed and tested in a low-speed wind-tunnel. The variation in scale of the models provides some insight into the rather severe Reynolds number effects, and the development of the smaller models provides an introduction into the difficulties in the design, manufacture and testing of small-scale vehicles.

The thrust is measured directly and compared with numerical predictions, with variations in the flapping motion, aspect-ratio and scale. Measured thrust for the larger model compares well with the numerical predictions both qualitatively and quantitatively over most of the parameter-space, however, the smaller model, with approximately half the chord-length and a somewhat different flapping motion, produces drastically different performance, indicating the presence of massive flow separation. The presented results indicate the necessity to better understand, and ultimately to utilize, flow separation in the design of successful flapping-wing MAVs.

Nomenclature

AR = aspect ratio, b/c
b = wing span
c = chord length
C_d = drag coefficient per unit span, $D/(q_\infty c)$
C_l = lift coefficient per unit span, $L/(q_\infty c)$
C_m = moment coefficient per unit span, $M/(q_\infty c^2)$
C_p = power coefficient per unit span, $-C_l \dot{y} - C_m \dot{\alpha}$
C_t = thrust coefficient per unit span, $T/(q_\infty c)$
D = drag per unit span

f = frequency in Hertz
h = plunge amplitude in terms of c
h_{te} = plunge amp. of the trailing edge in terms of c
k = reduced frequency, $2\pi f c / U_\infty$
L = lift per unit span
M = moment per unit span
q_∞ = freestream dynamic pressure, $1/2\rho_\infty U_\infty^2$
R_L = chord Reynolds number, $U_\infty c / \nu_\infty$
S = wing area
St = Strouhal number, $k h_{te}/\pi$
t = time
T = thrust per unit span $(-D)$
U_∞ = freestream velocity
x_p = pivot location from LE in terms of c
$y(\tau)$ = vertical displacement in terms of c
α = angle of attack
$\Delta\alpha$ = pitch amplitude in degrees
ϕ = phase between pitch and plunge
η = propulsive efficiency, C_t/C_p
ν_∞ = freestream kinematic viscosity
ρ_∞ = freestream density
τ = nondimensional time, tU_∞/c
$(\dot{\ })$ = rate of change w.r.t. τ

Introduction

The use of flapping-wing propulsion dates back much further than the forms of propulsion considered to be *conventional* in today's mechanical world. Indeed, nature has predominantly selected flapping-wing propulsion as the optimal approach, however, whether this choice is one of organic constraints or one of optimal performance is an unsettled matter. Nevertheless, the fact that birds, insects and many sea creatures utilize flapping-wing propulsion with great success, at the very least, merits a thorough scientific investigation. Of course, this is primarily an academic argument to pursue the topic, one which, until recently, has chiefly relegated flapping-wing research to something like a hobby-status. The necessary financial support for more dedicated research has recently come about as a result of interest in the development of Micro Air Vehicles (MAVs). The efficiency of conventional propellers diminishes rapidly with decreasing diameter promoting the search for alternative propulsive devices.

The scientific history of flapping-wing propulsion is rather lengthy, dating back nearly a century to the related but independent papers of Knoller[1] and Betz,[2] in 1909 and 1912, respectively. A more comprehensive summary of past work can be found in Jones and Platzer,[3] with a brief overview provided here for perspective.

Katzmayr[4] provided the first experimental verification of the Knoller-Betz effect in 1922, and a few years later Birnbaum[5,6] identified the conditions which lead to flutter or to thrust generation and suggested the use of a flapping wing as an alternative to the conventional propeller.

In 1935 von Kármán and Burgers[7] offered the first explanation of drag or thrust production based on the observed location and orientation of the wake vortices, as illustrated in Figs. 1 and 2 for drag-indicative and thrust-indicative wakes, respectively.
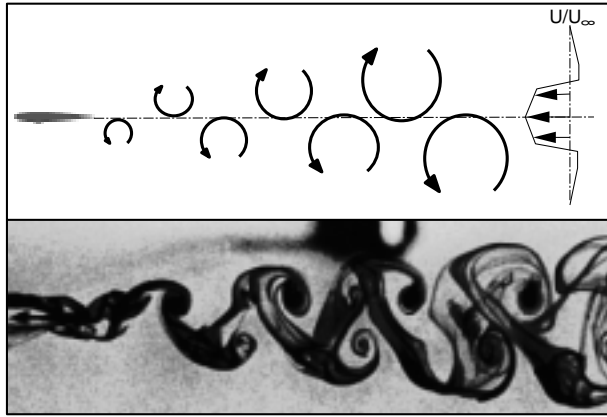
Fig. 1: Drag-indicative vortex street.[8]
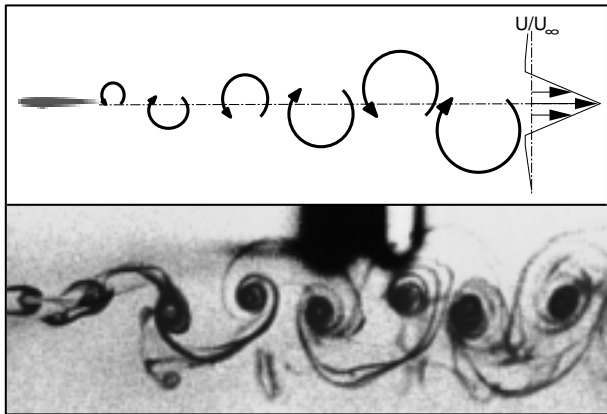
Fig. 2: Thrust-indicative vortex street.[8]

In 1936 Garrick[9] applied Theodorsen's inviscid, incompressible, oscillatory, flat-plate theory[10] to the determination of the thrust force providing the first notable numerical predictions of the thrust force, and in 1939, Silverstein and Joyner[11] provided the first experimental verification of Garrick's predictions.

In 1950 Bratt[12] performed flow visualization experiments which corroborated von Kármán and Burgers' observations. Of particular interest, Bratt's experimental data included several cases where a nonsymmetrical, deflected wake pattern was recorded, but no comment was made on these deflected wakes, and, in fact, they were never again reported until Jones et al[8] where they were shown to be reproducible both numerically and experimentally.

Birnbaum's suggestion to regard a flapping foil as an alternative (two-dimensional) propeller generated some interest over the years. Most noteworthy is Kuchemann and Weber's book[13] in which they comment on aerodynamic propulsion in nature and observe that the propulsive efficiency of an idealized flapping wing is greater than that of a simplified propeller model because of the disadvantageous trailing vortex system generated by the propeller.

It was recognized that at reasonable frequencies a large portion of the energy used to flap the airfoil was lost in the form of vorticity shed in the wake, and in 1942 Schmidt[14] surmised that a stationary wing placed in the oscillatory wake of a flapping wing could recover some of the vortical energy released from a flapping airfoil in the form of additional thrust.

In 1977, Bosch[15] developed a linear theory for predicting propulsion from flapping airfoils and airfoil combinations, for the first time including wake interference effects in propulsive efficiency computations. However, his linear approach modeled the wake as a vortex sheet confined to the plane of the airfoil, and therefore did not include the effect of the location of vortical structures on the interference effects, which, in general, lead to additional losses in efficiency.

In 1982 DeLaurier and Harris[16] obtained experimental measurements of flapping-wing propulsion. More recently, the problem of flapping foil propulsion has been considered by Liu[17,18] using vortex lattice and panel methods, by Send[19,20] using linearized theory and by Hall and Hall[21] and Hall et al[22] using vortex lattice methods.

Jones et al[8] compared wake structures behind flapping wings experimentally photographed and numerically predicted, and demonstrated that the formation and evolution of these unsteady wakes is essentially an inviscid phenomenon over a broad range of Strouhal numbers. Jones and Platzer[23] performed extensive numerical flapping-wing propulsion calculations using panel methods, and found a large performance enhancement for an airfoil flapping in ground effect, an effect often utilized by birds. In a further study they directly compared numerical predictions with experimental measurements for several flapping-wing configurations.[3]

Approach

In this section the previously developed numerical model is outlined, the configurations and relevant nomenclature are given and the experimental methods utilized for past and present experimental investigations are described. Additionally a brief overview of related past work by the present authors is given, providing key background information for the current work.

Numerical Methods

Flow solutions are computed using an unsteady, potential-flow code originally developed by Teng,[24] with additional features and a Graphical User Interface (GUI) developed by Jones and Center.[25]

The basic, steady panel code follows the approach of Hess and Smith,[26] where the airfoil is approximated by a finite number of panels, each with a local, uniform, distributed source strength and all with a global, uniform, distributed vorticity strength. For n panels there are n unknown source strengths, q_j, and an unknown vorticity strength, γ. Boundary conditions include flow tangency at the midpoint of the n panels and the Kutta condition which postulates that the pressure on the upper and lower surfaces of the airfoil at the trailing edge must be equal.

The unsteady panel code adopts the procedure of Basu and Hancock,[27] where a wake panel is attached to the trailing edge through which vorticity is shed into the flow. The Helmholtz theorem states that the total vorticity in a flow remains constant, thus a change in circulation about the airfoil must result in the release of vorticity into the wake equal in magnitude and opposite in direction, given numerically by

$$\Delta_k (\gamma_W)_k + \Gamma_k = \Gamma_{k-1} \qquad (1)$$

where Δ is the wake panel length, γ_W is the distributed vorticity strength on the wake panel and Γ is the circulation about the airfoil, and where the subscript k indicates the current time step, and $k-1$ indicates the previous time step.

The wake panel introduces two additional unknowns; the wake panel length and its orientation, θ_k, requiring two additional conditions for closure;

1. The wake panel is oriented in the direction of the local resultant velocity at the panel midpoint.
2. The length of the wake panel is proportional to the magnitude of the local resultant velocity at the panel midpoint and the time-step size.

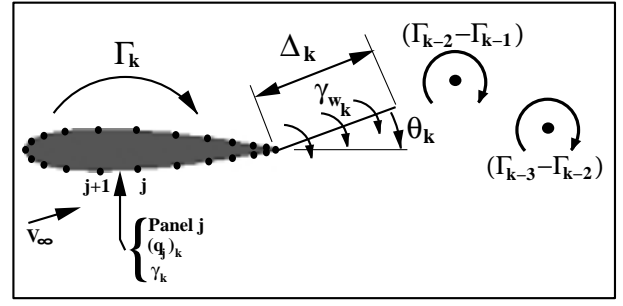The essential elements of this scheme are summarized in Fig. 3.

Fig. 3: Schematic of the panel code wake model.

At the end of each time step the vorticity contained in the wake panel is concentrated into a point vortex which is shed into the wake and convected downstream with the flow, influencing and being influenced by the other shed vortices and the airfoil. Note, implementation of this approach requires an iterative scheme, since the velocity direction and magnitude used to define the wake panel are not initially known. Note also that this wake model is nonlinear. The panel method was extended to a two airfoil system by Pang[28], allowing for the computation of wake interference phenomenon. The unsteady panel code has been extensively documented in Refs. 3, 8, 23-25 and 28-33.

Configurations and Nomenclature

The general equations of motion for the flapping wings are given in Fig. 4. All equations are non-dimensional, using the airfoil chord as the reference length and the freestream velocity as the reference speed.
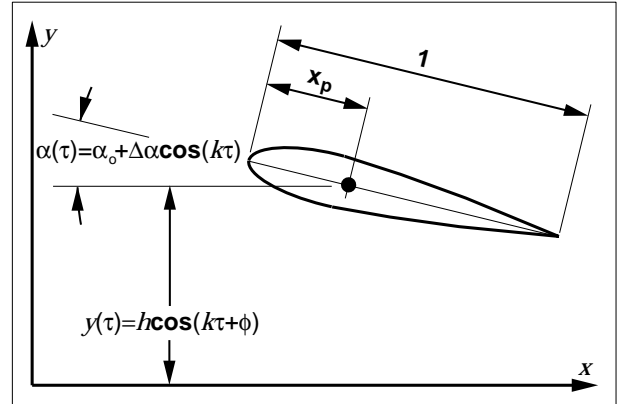

Fig. 4: Equations of motion & nomenclature.

Several configurations, shown in Fig. 5, have been considered in past and present research. The first is the simple, single flapping-wing configuration, the second is Schmidt's wave-propeller with the minor simplification of a pure plunging motion instead of Schmidt's circular flapping motion (the panel-code indicates minimal difference), the third configuration is the opposed-flapping configuration (or a single wing flapping near a

ground plane), the fourth configuration is an approximation to Schmidt's wave-propeller also utilizing the opposed plunge arrangement, and the fifth is really a pure-pitch motion, where the pitch axis is located some distance upstream. Note, only the vertically-symmetric configurations (c, d and e) have been tested experimentally, due to their balanced mechanical and aerodynamic loading, which allows the test models to remain quite steady even at rather high flapping frequencies, a feature which offers obvious advantages for a flying vehicle as well.
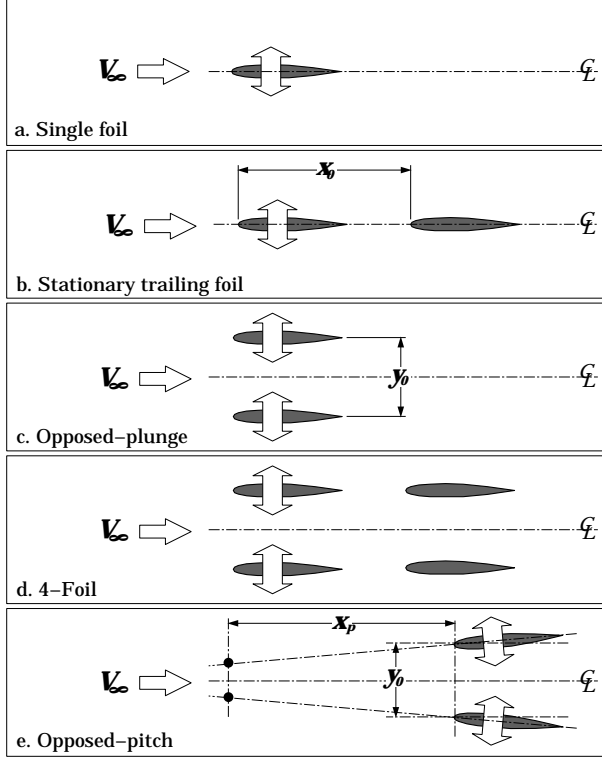

Fig. 5: Numerical and experimental configurations.

Overview of Past Research

A few key results from a previous paper (Ref. 3) are included here for clarity. The numerically predicted thrust coefficients for the first three configurations in Fig. 5 are shown in Fig. 6 with the numerically predicted propulsive efficiency plotted in Fig. 7. The flapping motions modeled the geometry of the experimental flapping mechanism, with a pure plunge motion in all cases, with $h = 0.4$ and $\alpha = 0$ degrees. For configuration (b) the LE-to-LE streamwise separation, x_0, was 1.2 chord lengths (numerically and experimentally very little dependence on the separation was found), and for configuration (c) the mean vertical separation between foils, y_0, was 1.4 chord lengths. For configuration (d), the values of x_0 and y_0 mentioned above were used.
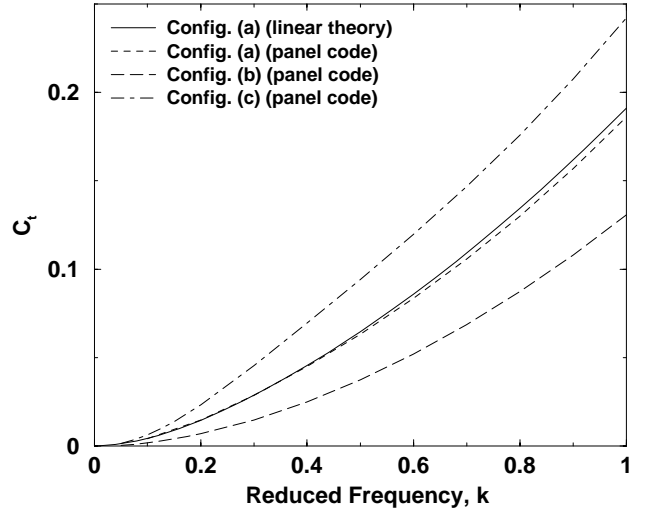

Fig. 6: Thrust coefficient versus reduced frequency.
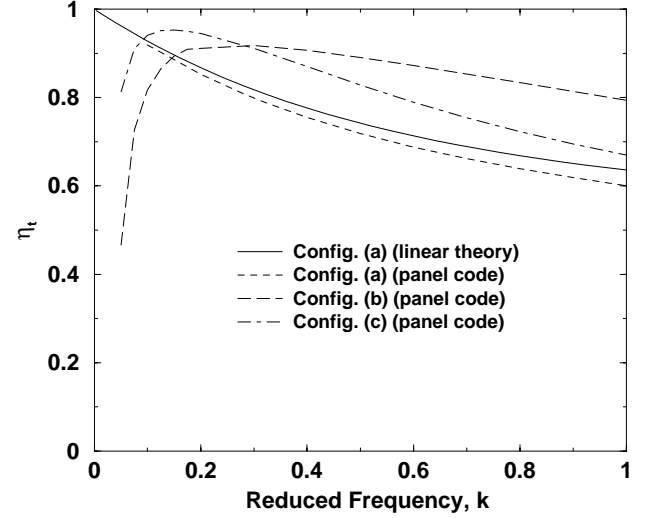
Fig. 7: Propulsive efficiency versus reduced freq.

The plotted thrust-coefficients for configurations (b) and (c) are the average values for the two airfoils. For configuration (b) the leading airfoil provides most of the thrust, but for configuration (c) the two foils contribute equally. The opposed-wing configuration yields significantly higher thrust coefficients, but configuration (b) appears to offer increased propulsive efficiency for most of the frequency range in agreement with Schmidt and Bosch (the apparent loss in efficiency at low frequencies is most likely false, due to numerical errors associated with the small singularity strengths). However, it's important to note that this is an inviscid analysis, and since configuration (b) is operating at a significantly lower thrust coefficient than the other configurations, its efficiency will be reduced much more by skin-friction losses. This is especially important on small-scale vehicles where profile drag coefficients may be quite large.

4

The computed and measured thrust values for configurations (c), (d) and (d) with tip-plates added are compared in Fig. 8. The presented results are for a flapping-frequency of 8 Hz, and the wings had a chord-length of $64mm$ and a span of $1270mm$.
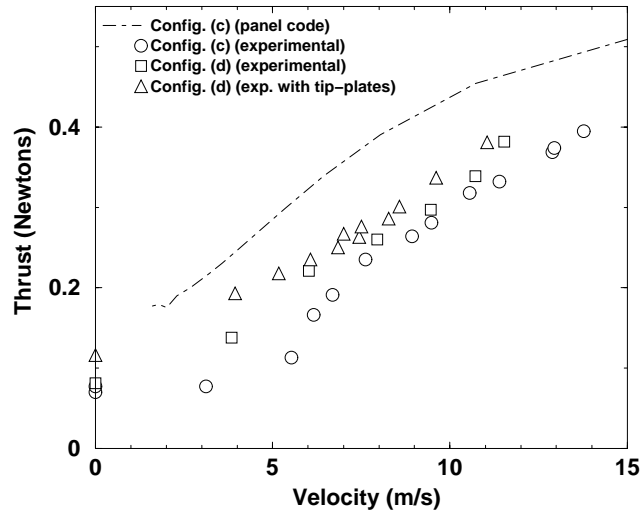

Fig. 8: Thrust versus velocity for configs. c and d.

All experimental results have had the drag removed. Since the drag is a function of wing position, the average drag while flapping at low frequency was used. Configuration (d) provided only a small increase in thrust, and since it had twice the wetted area of (c), the additional thrust did not offset the increase in drag. The exception was the low-speed range where (c) exhibited something like a drag bucket. The bucket extended to around $6m/s$ where the reduced frequency was about 0.5, the induced angle of attack due to the plunging motion had a magnitude of about 12 degrees and the chord Reynolds number was under 27,000. Presumably, the drag bucket was due to the onset of flow separation over part of the cycle.

Based on the relatively high thrust coefficient and propulsive efficiency and the good agreement between the experimental measurements and the numerical predictions, it was decided to pursue the opposed-plunge configuration (c) for the MAV.

Experimental Methods

For mechanical simplicity, a slight variation of the flapping motion was adopted for the MAV model, depicted in Fig. 5e. Instead of a pure plunge motion, a pure pitch motion is used, with the pitch axis several chord lengths in front of the wing. A cross-sectional drawing of the MAV is shown in Fig. 9, where the flow goes from left to right. An exploded view with one wing omitted and isometric and side views of the complete model are shown in Figs. 10, 11 and 12.
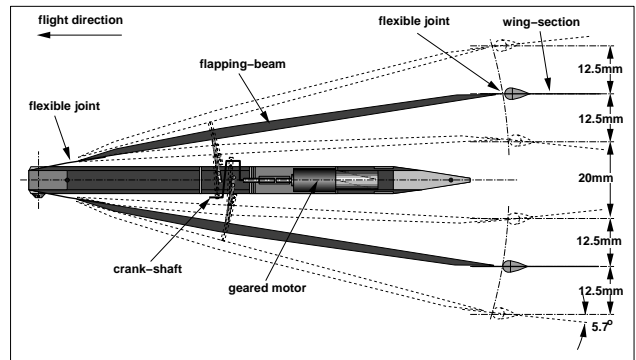
Fig. 9: Schematic of the 15cm MAV model.
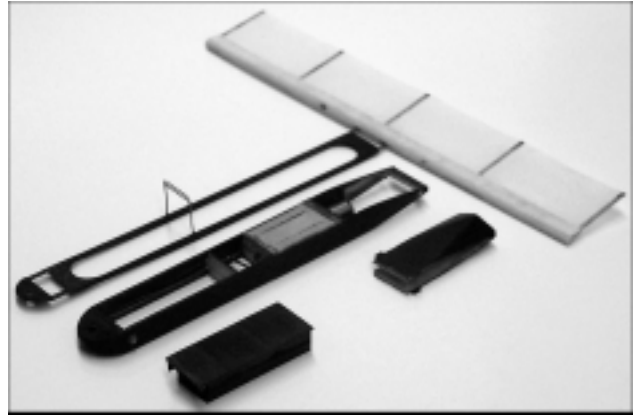
Fig. 10: Exploded view of the MAV.
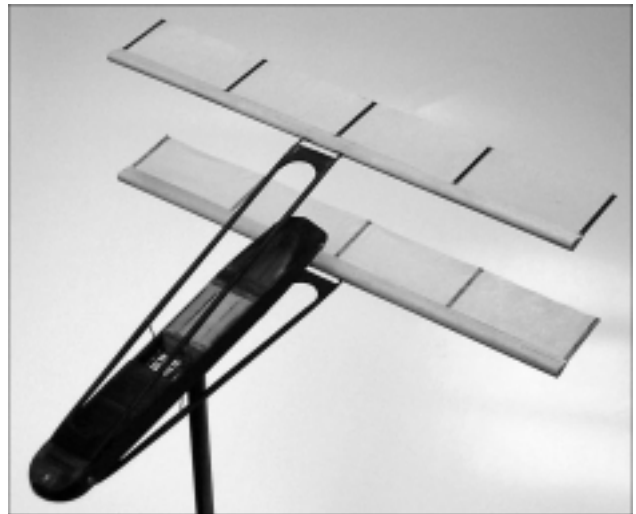

Fig. 11: Isometric view of the MAV.

Fig. 12: Side view of the MAV.

5

The models are designed around exceptionally small, geared, stepping motors from RMB Smoovy. The motors are $5mm$ in diameter and, with a 25:1 planetary gear system, they are about $25mm$ long. They weigh a meager $2.4g$ and produce a torque of about $2.5mNm$ at speeds up to about 800 RPM, which yields a maximum power of roughly 0.21 watts. The brushless motors are controlled by an oscillatory driver circuit, which allows for very precise, steady and reproducible rotational speeds. Presently, the control circuit and power supply are large and bulky, and must be external to the model. While the motor has a reported max speed of around 100,000 RPM, the gearbox is only rated for 20,000 RPM input, which limits the flapping speed to around 13 Hz, however, with some models, sustained speeds of over 15 Hz have been reached.

A very small crankshaft is coupled to the motor using thin-wall silicon tubing. The crankshaft moves the flapping-beams via Scotch yokes constructed of very thin piano wire. The mechanism takes some effort to construct, but has proven to be quite robust, and may easily be disassembled for maintenance or part substitutions.

The 3-pole power is fed into the model through four $0.076mm$ diameter copper wires that support the model. The support wires are attached to the model via small gold-plated pins, at the nose, and near the rear of the model. The mass of the wires is negligible compared to the mass of the model and the wires are flexible enough not to impede the model's motion. The model is suspended from the tunnel ceiling by the support wires such that the model may swing freely in the streamwise direction, but is relatively steady in all other directions, as shown in Fig. 13.

As the model flaps and creates thrust, the model is displaced in the streamwise direction, and the displacement is measured by bouncing a laser sensor off a small reflective surface on the back of the rear nacelle, as shown in Fig. 14. The laser analog sensor, an NAIS model ANL1651, is nominally $130mm$ downstream of the model, and measures distances accurately within the range 80 to $180mm$. The sensor is generally about 3 to 4 chord lengths downstream of the model and is not thought to create a significant flow interference effect. The accuracy of the sensor is prescribed by the manufacturer as $\pm 100\mu m \pm 0.002 \times \Delta x$ for the range $130mm \pm 35mm$. For some wing configurations, at higher frequencies the wings would completely come together in the middle, blocking the path of the laser to the reflective panel on the rear nacelle. In these cases an alternative rear nacelle was used that supported a small rectangular panel slightly downstream of the wing trailing edge.
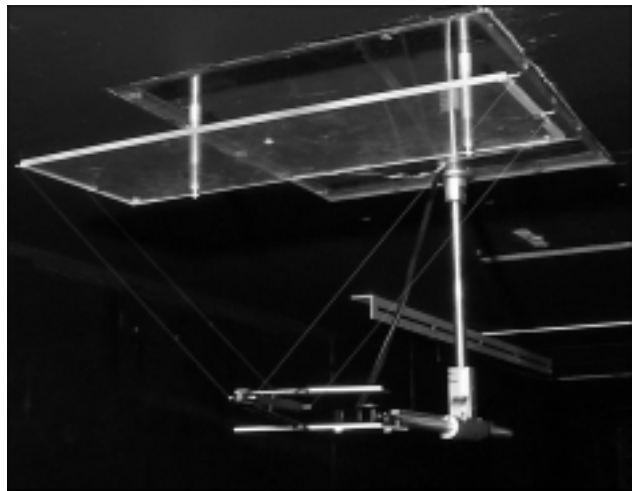
Fig. 13: The MAV mounted in the wind-tunnel.
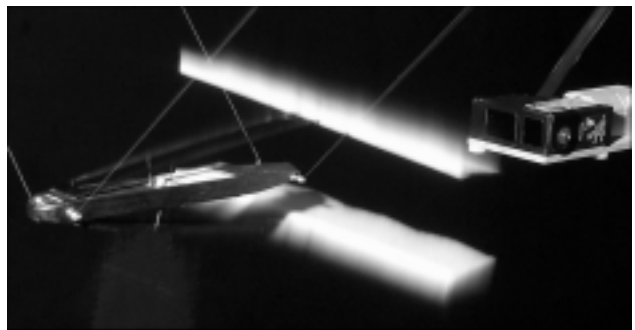
Fig. 14: The MAV, in action, with the Laser sensor.

The thrust is computed by measuring the precise mass of the model, the length of the pendulum, and the horizontal displacement due to thrust, and using the equation

$$T = \frac{W\Delta x}{\sqrt{L^2 - \Delta x^2}} \qquad (2)$$

where W is the MAV weight, L is the pendulum length and Δx is the horizontal deflection. The length was originally established such that the natural frequency would be 1Hz, however, the fragile wires break and/or detach from the pins occasionally or are elongated when over-stressed, so the natural frequency was periodically checked by perturbing the model and letting it swing sinusoidally with small amplitude. The displacement signal from the laser sensor was recorded on a digital storage oscilloscope for a 32 second period, and the length of time needed to complete 30 or 31 cycles was used to compute the pendulum length where

$$L = \frac{g}{(2\pi f)^2}. \qquad (3)$$

Assuming that the determination of the peaks of the first and last cycle in the sampled data can be determined within 5%, the error in the period is about

0.17%, which corresponds to a length error of about 0.33% in Eq. 3.

To reduce the deflection of the pendulum (in order to keep the model in the more accurate range of the laser sensor) ballast is added to the model. The dry mass of the MAV is typically about 6 grams, depending on the set of wings used, and the ballast (the black box in the bottom left corner of Fig. 10) adds about 11 grams. The model mass is measured on a Setra EL410D digital balance with a $0.001g$ accuracy. The model mass may actually vary by about $0.005g$ from day to day, due to humidity, dust and other environmental contamination.

The model has a composite construction, built primarily out of balsa-wood and very thin graphite-epoxy laminates. The wings are constructed using tear-drop shaped balsa leading edges with thin carbon-fiber ribs, and the surfaces are made from very light-weight Japanese tissue. Typical wing masses are about 0.3 grams. The wings are attached to the flapping-beams using thin carbon fiber strips, with the length and width of the strip varied to control the elasticity of the joint. Super-glue is used to attach the carbon fiber strips to the flapping beams in such a way that the wings may easily be removed. The static, mean angle of attack of the wings is adjusted by heating the carbon fiber strips with a soldering iron, which softens the epoxy and allows the strips to bend. Upon cooling they retain their new shape. The elasticity of the wing mount allows for a passive feathering mechanism. The wing deflects in pitch proportionally to the moment about the leading edge. The addition of this feature boosts static performance significantly and generally allows the motor to reach higher frequencies, since it reduces the peak torque requirements.

The initial wing geometry had a span of $150mm$ and a chord of $25mm$, but a variety of additional wings have been built to investigate chord-length and aspect-ratio effects. Wings with constant wing area and aspect ratios of 3, 6 and 12 are shown in Fig. 15. Wings with a fixed chord of $36mm$ and spans of 105, 150 and $200mm$ are shown in Fig. 16.

The flapping frequency is measured using a strobe light. The strobe light is set to a specific frequency, and the motor speed is adjusted until the wing motion appears frozen in the light of the strobe. The stepping-motor/controller circuit provides very precise, incremental speed control, and the motor-speed is completely constant during a simulation, a feature that is typically not possible with conventional brushed motors.

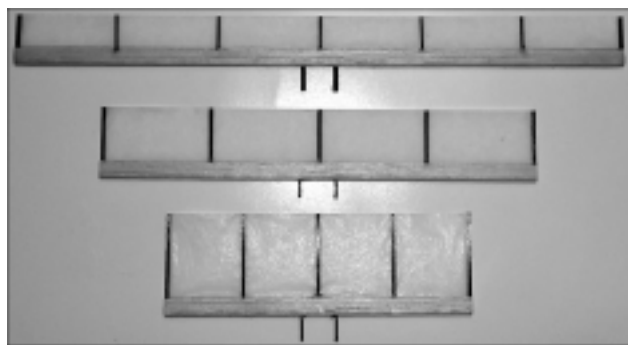Experiments are performed in the Naval Postgraduate School $1.5 \times 1.5m$ low-speed wind-tunnel, shown in Fig. 17.
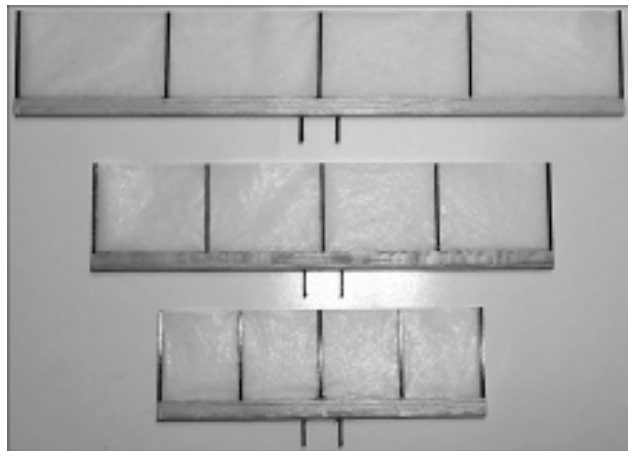

Fig. 15: Constant area, variable AR wings.

Fig. 16: Constant chord, variable span wings.
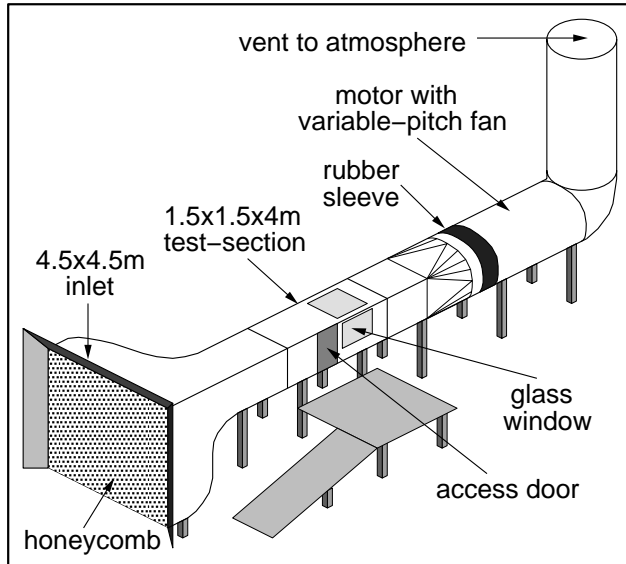

Fig. 17: The NPS low-speed wind tunnel.

The tunnel, modeled after the one described in Ref. 34, is a continuous, flow-through facility with an approximate flow speed range between $0m/s$ and $10m/s$. The speed is set by varying the pitch of a fan which is driven by a constant speed motor. The tunnel has a square, $4.5 \times 4.5m$, bell-shaped inlet with a 9-to-

7

1 contraction ratio to the $1.5 \times 1.5m$ test section. The turbulence level has been determined by Costello[35] using a hot-wire anemometer. In the speed range from $2m/s$ to $10m/s$ the highest level was 0.97% and the lowest level was 0.47%.

Flow speed in the tunnel is measured using a pitot-static tube at the upstream end of the test-section, attached to an MKS Baratron type 223B differential pressure transducer. The transducer provides a voltage that is linear with the differential pressure, yielding 1 volt at 1 torr. The flow-speed is then given by

$$U_\infty = \sqrt{\frac{2\Delta p}{\rho_\infty}} \qquad (4)$$

The transducer has a reported accuracy of 0.5% of the full-scale reading which, due to the nature of Eq. 4, results in rather large errors in the measurement of low velocities but quite small errors in the measurement of high velocities. LDV equipment will soon be available for more accurate low-speed measurements as well as time-accurate localized velocity measurements of the surrounding flowfield.

The pitot-static tube has errors associated with the measurement of both the static and total pressure. The pitot tube used here has an outer diameter of $8mm$, 8 static ports aligned symmetrically, $64mm$ (8 diameters) downstream of the tip base, and a stem approximately $120mm$ (15 diameters) downstream of the static ports. According to Pope,[36] the geometry of the probe should yield about an 0.5% over-prediction of the static pressure.

The above mentioned errors are shown in the form of error-bars in the included results. Additionally, several readings of each data point are taken, and the average deviation of the recorded data is combined with the estimated accuracy of the measurement, providing insight into the reliability of the data.

For oscillatory motions the reduced frequency and/or Strouhal number are generally the significant non-dimensional parameters. Reduced frequencies between about 0.1 to 10 are tested, as well as the limiting case of static thrust that yields a theoretical reduced frequency of infinity (based on free-stream speed). The Reynolds number is not of great importance to this investigation (other than its unknown role in flow separation), but it varied roughly between 0 and 17,500, based on chord length.

Results

Unfortunately, our 50 year old windtunnel was down for mandatory maintenance until just a few weeks before this paper was presented. Consequently, a greater portion of the results presented here are for the static

case, with $U_\infty = 0$. This is actually an interesting problem in itself, but as it turns out, the ideal design for static thrust may not be the ideal design for the non-static case.

The configuration of the MAV is somewhat variable. As previously mentioned, the wings may easily be changed, as well as the stiffness of the wing mount. However, the basic geometry of the flapping mechanism is not so easily modified. The MAV fuselage requires a substantial effort to build, and the design does not easily allow for changes in the flap amplitude and the mean separation of the wings. The final design is a compromise between what was good numerically and what could reasonably be built and driven. The original design used wings with a span of $150mm$ and a chord of $25mm$, and the flapping mechanism resulted in a plunge amplitude of $12.5mm$ ($h = 0.5$) and a pitch amplitude of 5.7 degrees (recall that the motion is really a pure pitch motion about an axis far upstream of the leading edge, which is nearly the same as a coupled pitch and plunge motion that are 180 degrees out of phase).

Using the panel code, the predicted thrust as a function of velocity and frequency was computed for the design geometry, as shown in Fig. 18. The performance followed the trend predicted by linear theory for a single airfoil, with the thrust at high velocity roughly double the static thrust, and with the thrust increasing as roughly the square of the frequency.
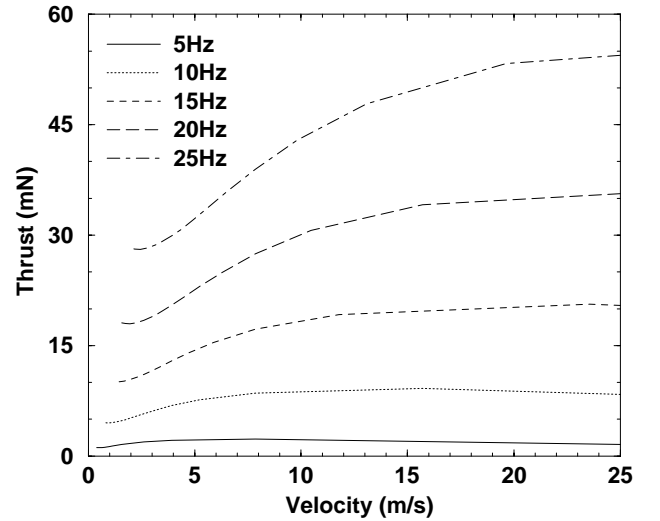

Fig. 18: Numerical prediction of performance.

The out-of-phase pitch-plunge motion is not ideal but, as previously mentioned, was selected because of its mechanical simplicity. The effect of going from a pure plunge to the coupled pitch-plunge is illustrated in Fig. 19. A reduced frequency of 1 is used, with the plunge amplitude of the leading edge fixed at $0.5c$, and the pitch amplitude varied between 0 degrees (the

pure plunge case) and 10 degrees. Interestingly, the thrust actually increases with pitch amplitude, but at a loss in efficiency. Nominally the MAV operates with $\Delta\alpha = 5.7$ degrees, but with the elastic wing mounts, the wings tend to feather with something closer to a 90 degree phase angle. No attempt has been made thus far to model the elastic configuration numerically. While this may be possible, using a previously developed aeroelastic capability (see Ref. 37), it may be of little use, as the elastic deflection is most likely responding to separation effects which cannot be modeled by the panel code.
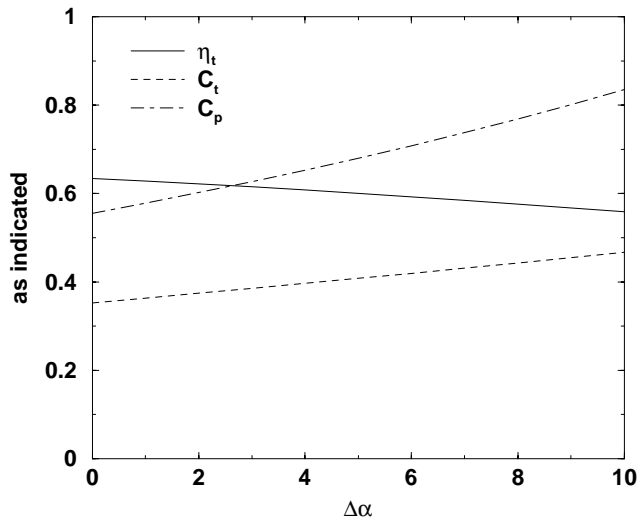

Fig. 19: Effect of pitch amplitude.

The airfoil sections used on the MAV are rather unconventional, not by choice, but because of weight restrictions and the difficulty in producing more common airfoils. Of course, the Reynolds numbers are very low, and the dynamic angles of attack very high, so the choice of airfoils is not obvious. Therefore, a substantial effort was made to find a suitable airfoil shape and construction. In Fig. 20 the measured static thrust ($U_\infty = 0$) is plotted for a few of the airfoils tested.

The first had essentially a rectangular leading edge built from a thin layer of balsa wood sandwiched between laminations of carbon-fiber. The leading edge was extremely stiff, but not all that light, and not an ideal shape for high angles of attack. The second was the lightest wing, with an airfoiled balsa leading edge about the same size as the rectangular leading edge. Due to its light weight, the wings could be flapped faster, but produced virtually identical thrust to the first case. The third case, which is now used on all wings, used a much larger airfoiled balsa leading edge. Balsa varies in density by several hundred percent from piece to piece, and by being very selective, very light wings with this airfoiled leading edge have been built. Since the balsa leading edge comprises around two

thirds of the wing weight, it was thought that a cylindrical leading edge might perform just as well, and be a little lighter. However, the performance was not quite as good, and the weight difference was too small to help much.
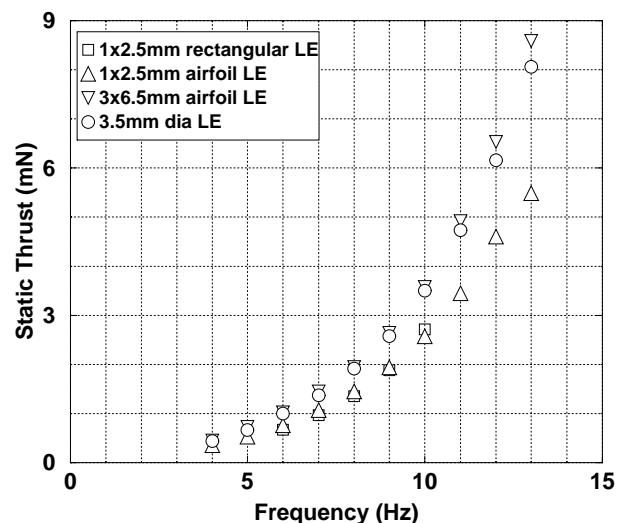

Fig. 20: Effect of leading-edge shape.

It is thought that the improved performance for the larger airfoiled leading edge is due in part to a thicker, rounded leading edge, although the surface roughness is still quite large. Additionally, the present wing design has an aeroelastically changeable camber, due to the flexibility of the this graphite ribs. Unfortunately, the camber deflects in the less desirable direction, at least based on conventional airfoil theory. Some work has gone into the development of wings with passive camber changes, with the camber moving in the correct direction, but data are not yet available for those wings.

Some effort has been made to evaluate the flow quality over these sections, but on this scale, this is not a simple task. Use of standard fog machines has provided some insight, however, the fog particles alter the flow density, and if the fog hits the left or right or top or bottom of the MAV unevenly, the model is fairly violently thrown around due to the differential lift and thrust. The newest fuselage incorporates a rigid mount capability (as shown in Figs. 11 and 12), and this may provide a better means for future flow visualization studies.

Additionally, tufts have been used on some of the wings with varying success. With the very short lengths and the very energetic motions involved, the material selection for the tufts becomes difficult. Using a single strand of standard cotton thread (it is usually made of 3 or 4 thinner strands wound together), and varying lengths and placements, some data has been

obtained. However, the cotton fibers tend to stick to the tissue surface, and they must be manually freed. Additionally, the proper length is an unknown. If the tufts are too short then the stiffness of the material may prevent the tufts from moving with the flow, and if they are too long they may indicate inertial effects rather than the local flow.

In Fig. 21 the performance is plotted for several wings with varying aspect ratio but a constant wing area. The design aspect ratio was 6, and wings with aspect ratio 3 and 12 were also tested. Since the wing area was fixed, any changes in measured thrust reflect directly on the performance of the configuration. The aspect ratio 3 case yields lower thrust, but the other two are virtually identical.
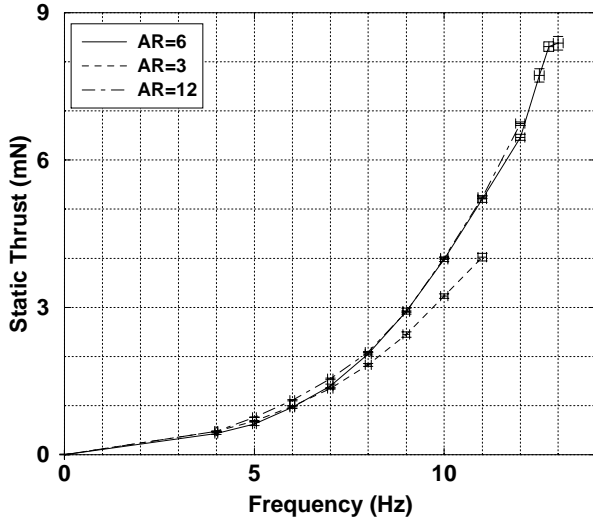

Fig. 21: Effect of aspect ratio (fixed wing-area).

Unfortunately, due to the fixed geometry of the motion, the three wings in Fig. 21 all had different values of c, h, k and the mean separation, as well as differing aspect ratios. However this difference indicates that the chord and mean separation for the aspect-ratio 6 and 12 wings have minimal effect (unless they are offsetting).

A further test of aspect-ratio sensitivity was made, fixing the chord ($36mm$) and altering the span, such that c, h, k and the mean separation were all the same, but the wing area varied. In Fig. 22 the thrust is plotted, but with the thrust of the $105mm$ and $200mm$ wings scaled so that all assume a unit wing area equivalent to the $150mm$ span wing.

Here again, the two large aspect-ratio cases ($AR = 4.17$ and $AR = 5.56$) provide virtually identical results, but the low aspect ratio case yields considerably lower results. Unfortunately, this too is not an ideal test case, as the differing wing areas provided different moments about the leading edge, resulting in different aeroelastic deflections of the wings.
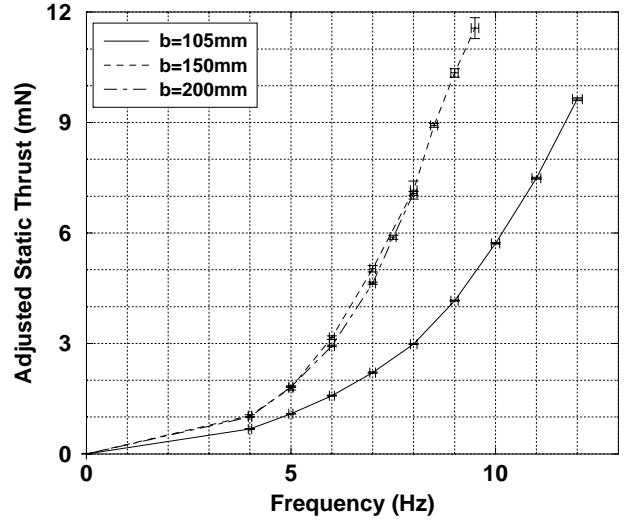

Fig. 22: Effect of aspect ratio (fixed chord).

The remaining data includes a few sets obtained after the repair of the windtunnel. In Fig. 23 the thrust predicted by the panel code and measured experimentally are compared for the design configuration with $b = 150mm$, $c = 25mm$ and a fairly rigid wing mount for two frequencies, 8 and 12Hz.
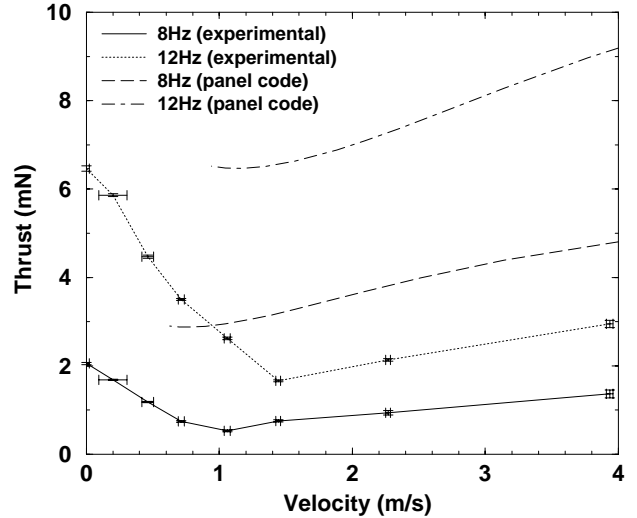

Fig. 23: Thrust for the $150 \times 25mm$ wing.

The panel code is unable to compute the static case for several reasons. First, the static case corresponds to an infinite reduced frequency, and second, the panel code assumes fully attached flow which may be a poor assumption for the MAV altogether, but it is certainly wrong at high reduced frequencies. Even at a reduced frequency of 2, the lowest velocity shown in the figure, the numerical results become questionable. Extrapolating the numerical values to the static case seems to agree pretty well with the measured thrust. However, when the tunnel is turned on, the perfor-

mance of the MAV drops off quickly, but begins to recover at higher speeds. The behavior is quite different from the panel code predictions, but may indicate something like the drag bucket experienced in Ref. 3.

More complete data sets for the configuration described above and for a configuration with a span of $150mm$ and a chord of $36mm$ are shown in Figs. 24 and 25, respectively. A similar shape is seen for all frequencies, with a rapid decline in thrust at low speeds, followed by a partial recovery after a minimum value.
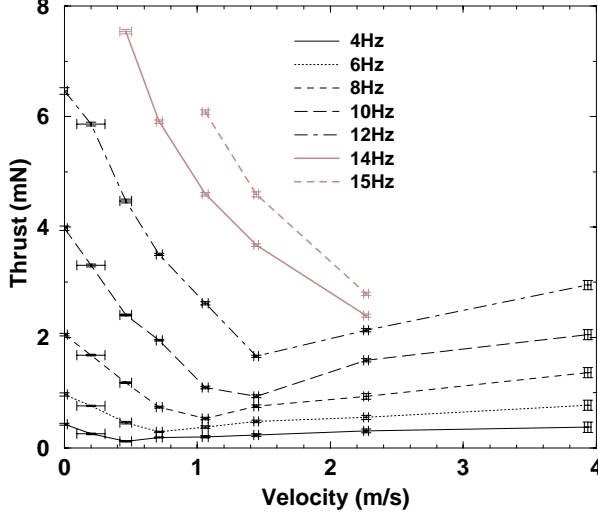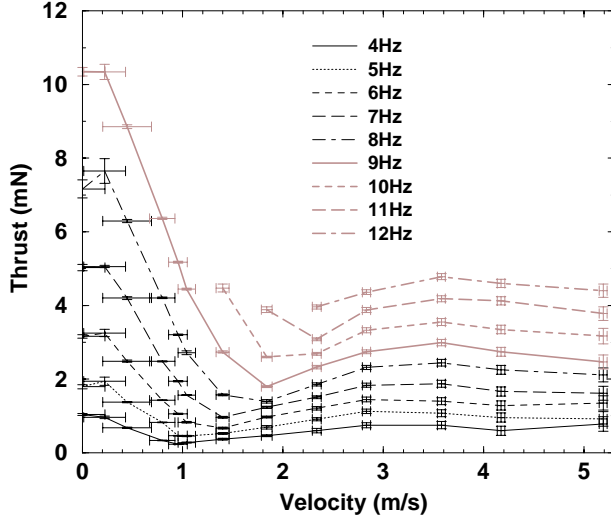

Fig. 24: Thrust for the $150 \times 25mm$ wing.

Fig. 25: Thrust for the $150 \times 36mm$ wing.

The speed where the minimum thrust occurs increases with frequency but, interestingly, occurs at approximately the same reduced frequency for a configuration (about 1.2 for the first case, and 1.1 for the second case), and in both configurations the Strouhal number at the minimum is about 0.23. Note, for the Strouhal number the reference length is the wake half-width, which must be approximated to include the

elastic deflection of the wings. The Strouhal number is a good indication of the induced angle of attack ($\alpha_i \approx \tan^{-1}(St\pi)$), with a Strouhal number of 0.23 indicating an induced angle of attack of around 36 degrees. It's fair to assume that the flow is fully detached, and most likely the convection rate of the dynamic-stall vortex places it in a highly disadvantageous position. On the other hand, in the static case, the dynamic stall vortex probably convects much more slowly, due primarily to the entrained flow, and actually appears to aid in the propulsive performance. Clearly, a better understanding of the development and motion of the dynamic-stall vortices is required for the design of a successful flapping-wing MAV.

The second configuration has a larger wing area and more flexible wing joints, so it feathers much more than the first configuration. Consequently, in agreement with the panel code, its thrust is higher in the static case but diminishes at higher speeds.

Conclusions & Prospective

An investigation of flapping-wing propulsion on scales suitable for Micro Air Vehicles (MAVs) was performed. The numerical and experimental results obtained from several previous studies influenced the design of a $15cm$ MAV test model; however, the small size and stringent weight criteria required a compromise for design simplicity and mechanical efficiency. Specialized construction techniques, materials and testing equipment were required to assemble, power and test the 6 gram models. Experiments were performed in the Naval Postgraduate School $1.5m \times 1.5m$ low-speed wind tunnel in the speed range of 0 to $5m/s$. The effect of several of the many variables in the parameter space were investigated, as well as the effects of leading-edge radius and airfoil quality. Thrust was measured directly and compared with numerical predictions.

The wind-tunnel was non-functional until late in the study, so all early experiments were static (wind off). The static testing provided the necessary experience to optimize the mechanics of the model and work out most of the bugs in the testing equipment. Additionally, static testing helped to refine the airfoil shape and construction. Tests indicated that leading-edge radius played an important role in the performance, with increased performance for thicker leading edges. The selected design incorporated a $3 \times 6.5mm$ teardrop shaped leading edge spar with a membrane wing surface supported by several graphite ribs. Static tests with varying aspect ratio found that performance decreased for aspect ratios lower than about 4.5, but remained essentially fixed above that value.

While the static performance of the test configurations matched the numerical model quite well, the wind-on performance diverged quickly from the numerical predictions, most likely indicating the presence of massive separation. Interestingly, separation was expected in the static case, where agreement with the panel code was good, and at higher speeds where the flow might reattach, the comparison with the panel code was far worse. The minimum thrust for both configurations and all tested frequencies occurred at a Strouhal number of about 0.23, which indicated an approximate induced angle of attack of 36 degrees. At lower speeds, where the induced angle of attack was even higher, the performance increased. The positioning of the dynamic-stall vortices apparently was favorable in the static and very low-speed region, but very unfavorable at higher-speeds. Clearly a better understanding of the development and evolution of the dynamic-stall vortices is required for a successful flapping-wing MAV.

Based on this, future studies are planned to investigate in more detail the complex structure of the flowfield. The experimental results from the previous publication (Ref. 3) showed that the larger flapping model produced results in good qualitative and quantitative agreement with the panel code. However, the MAV, operating at roughly half the Reynolds number, demonstrates quite different performance characteristics. Flow visualization using flow-seeding and tufts are underway for both the large and small model, and LDV will be used to obtain detailed maps of the unsteady flowfields. Some equipment modifications need to be done in order to test the MAVs at higher flow speeds, but the trends for the more rigid wing model are encouraging. Unfortunately, the results presented in Figs. 24 and 25 were all in the Strouhal number range where the drag-bucket was present for the larger model. Therefore, it is hoped that the performance characteristics predicted by the numerical model and measured with the larger model at higher speeds may be achieved with the MAV model as well. Additionally, more sophisticated models are under development that incorporate limited pitch control to obtain a pure plunge motion, instead of the less optimal pitch-plunge motion currently used, and others that use passive camber control of the wing surface.

Acknowledgments

References

[1] Knoller, R., "Die Gesetze des Luftwiderstandes," **Flug- und Motortechnik (Wien)**, Vol. 3, No. 21, 1909, pp. 1-7.

[2] Betz, A., "Ein Beitrag zur Erklärung des Segelfluges," **Zeitschrift für Flugtechnik und Motorluftschiffahrt**, Vol. 3, Jan. 1912, pp. 269-272.

[3] Jones, K. D. and Platzer, M. F., "An Experimental and Numerical Investigation of Flapping-Wing Propulsion," AIAA Paper No. 99-0995, Reno Nevada, Jan. 1999.

[4] Katzmayr, R., "Effect of Periodic Changes of Angle of Attack on Behavior of Airfoils," NACA Report No. 147, Oct., 1922. (translated from **Zeitschrift für Flugtechnik und Motorluftschiffahrt**, March 31, pp. 80-82, and April 13, 1922, pp. 95-101).

[5] Birnbaum, W., "Das ebene Problem des schlagenden Flüels," **Zeitschrift für Angewandte Mathematik und Mechanik**, Vol. 4, No. 4, Aug., 1924, pp. 277-292.

[6] Birnbaum, W., "Der Schlagflügelpropeller und die kleinen Schwingungen elastisch befestigter Tragflügel," **Zeitschrift für Flugtechnik und Motorluftschiffahrt**, Vol. 15, 1924, pp. 128-134.

[7] Von Kármán, T. and Burgers, J. M., "General Aerodynamic Theory - Perfect Fluids," Division E, Vol. II, Aerodynamic Theory, Ed. Durand, W. F., 1943, p. 308.

[8] Jones, K. D., Dohring, C. M. and Platzer, M. F., "Experimental and Computational Investigation of the Knoller-Betz Effect," **AIAA Journal**, Vol. 36, No. 7, May 1998.

[9] Garrick, I. E., "Propulsion of a Flapping and Oscillating Airfoil," NACA Report 567, 1936.

[10] Theodorsen, T., "General Theory of Aerodynamic Instability and the Mechanism of Flutter," NACA Report No. 496, 1935.

[11] Silverstein, A. and Joyner, U. T., "Experimental Verification of the Theory of Oscillating Airfoils," NACA Report No. 673, 1939.

[12] Bratt, J. B., "Flow Patterns in the Wake of an Oscillating Airfoil," Aeronautical Research Council, R&M 2773, 1953.

[13] Kuchemann, D. and Weber, J., "Aerodynamic Propulsion in Nature," Chapter 11, *Aerodynamics of Propulsion*, McGraw Hill Book Co., New York, 1953, pp. 248-260.

[14] Schmidt, W., "Der Wellpropeller, ein neuer Antrieb fuer Wasser-, Land-, und Luftfahrzeuge," Z. Flugwiss. Vol. 13, 1965, pp. 472-479.

[15] Bosch, H., "Interfering Airfoils in Two-dimensional Unsteady Incompressible Flow," AGARD CP-227, Paper No. 7, Sept. 1977.

[16] DeLaurier, J. D. and Harris, J. M., "Experimental Study of Oscillating-Wing Propulsion," **Journal of Aircraft**, Vol. 19, No. 5, May, 1982, pp. 368-373.

[17] Liu, P., "Three-Dimensional Oscillating Foil Propulsion," Masters Engineering Thesis, University of Newfoundland, march, 1991.

[18] Liu, P., "A Time-Domain Panel Method for Oscillating Propulsors with Both Chordwise and Spanwise Flexibility," Ph.D. Thesis, University of Newfoundland, 1996.

[19] Send, W., "The Mean Power of Forces and Moments in Unsteady Aerodynamics," **Zeitschrift für Angewandte Mathematik und Mechanik**, Vol. 72, 1992, pp. 113-132.

[20] Send, W., "Otto Lilienthal und der Mechanismus des Schwingenflugs," DGLR-JT96-030, German Aerospace Congress, Dresden, Sept., 1996.

[21] Hall, K. C. and Hall, S. R., "Minimum Induced Power Requirements for Flapping Flight," *Journal of Fluid Mechanics*, Vol. 323, Sept., 1996, pp. 285-315.

[22] Hall, K. C., Pigott, S. A. and Hall, S. R., "Power Requirements for Large-Amplitude Flapping Flight," AIAA Paper No. 97-0827, Jan., 1997.

[23] Jones, K. D. and Platzer, M. F., "Numerical Computation of Flapping-Wing Propulsion and Power Extraction," AIAA Paper No. 97-0826, 1997.

[24] Teng, N. H., "The Development of a Computer Code for the Numerical Solution of Unsteady, Inviscid and Incompressible Flow over an Airfoil," Master's Thesis, Naval Postgraduate School, Monterey, CA, June 1987.

[25] Jones, K. D. and Center, K. B., "Numerical Wake Visualization for Airfoils Undergoing Forced and Aeroelastic Motions," AIAA Paper No. 96-0055, Jan., 1996.

[26] Hess, J. L. and Smith, A. M. O., "Calculation of Potential Flow about Arbitrary Bodies," **Progress in Aeronautical Sciences**, Vol. 8, pp. 1-138, Pergamon Press, Oxford, 1966.

[27] Basu, B. C. and Hancock, G. J., "The Unsteady Motion of a Two-Dimensional Aerofoil in Incompressible Inviscid Flow," **Journal of Fluid Mechanics**, Vol. 87, 1978, pp. 159-168.

[28] Pang, C. K., "A Computer Code for Unsteady Incompressible Flow past Two Airfoils," Aeronautical Engineer's Thesis, Dept. of Aeronautics and Astronautics, Naval Postgraduate School, Monterey, CA, Sept. 1988.

[29] Platzer, M. F., Neace, K. S. and Pang, C. K., "Aerodynamic Analysis of Flapping Wing Propulsion," AIAA Paper No. 93-0484, Jan. 1993.

[30] Neace, K. S., "A Computational and Experimental Investigation of the Propulsive and Lifting Characteristics of Oscillating Airfoils and Airfoil Combinations in Incompressible Flow," Master's Thesis, Dept. of Aeronautics and Astronautics, Naval Postgraduate School, Monterey, CA, Sept. 1992.

[31] Tuncer, I. H., Platzer, M. F. and Ekaterinaris, J. A., "Computational Analysis of Flapping Airfoil Aerodynamics," ASME Fluids Engineering Division, Summer Meeting, June, 1994.

[32] Riester, P. J., "A Computational and Experimental Investigation of Incompressible Oscillatory Airfoil Flow and Flutter Problems," Master's Thesis, Naval Postgraduate School, Monterey, CA, June 1993.

[33] Turner, M., "A Computational Investigation of Wake-Induced Airfoil Flutter in Incompressible Flow and Active Flutter Control," Master's Thesis, Naval Postgraduate School, Monterey, CA, March, 1994.

[34] Ringleb, F. O., "The Three-Dimensional Smoke Tunnel of the Naval Air Engineering Laboratory in Philadelphia," Report. NAEL-ENG-6818, Jul. 1961.

[35] Costello, J. P. II, "Smoke and Helium Bubble Visualization Studies of Incompressible Flow Past a Jet-Flap Airfoil," Master's Thesis, Department of Aeronautics and Astronautics, Naval Postgraduate School, Monterey, CA, June 1972.

[36] Pope, A., Wind-Tunnel Testing, Second Edition, John Wiley & Sons, Inc., New York, 1954.

[37] Jones, K. D. and Platzer, M. F., "Time-Domain Analysis of Low-Speed Airfoil Flutter," **AIAA Journal**, Vol. 34, No. 5, May 1996.